fluids

MDPI

Article

Predictive Analysis of Structural Damage in Submerged Structures: A Case Study Approach Using Machine Learning

Alexandre Brás dos Santos [1,*], Hugo Mesquita Vasconcelos [1], Tiago M. R. M. Domingues [1], Pedro J. S. C. P. Sousa [1,2], Susana Dias [1], Rogério F. F. Lopes [1,2], Marco L. P. Parente [2], Mário Tomé [3], Adélio M. S. Cavadas [3] and Pedro M. G. P. Moreira [1]

[1] INEGI, Institute of Science and Innovation in Mechanical Engineering and Industrial Engineering, Campus da FEUP, R. Dr. Roberto Frias 400, 4200-465 Porto, Portugal
[2] Department of Mechanical Engineering, Faculdade de Engenharia, Universidade do Porto, R. Dr. Roberto Frias s/n, 4200-465 Porto, Portugal
[3] PROMETHEUS, School of Technology and Management (ESTG), Polytechnic Institute of Viana do Castelo, Avenida do Atlântico n° 644, 4900-348 Viana do Castelo, Portugal
[*] Correspondence: absantos@inegi.up.pt

Abstract: This study focuses on the development of a machine learning (ML) model to elaborate on predictions of structural damage in submerged structures due to ocean states and subsequently compares it to a real-life case of a 6-month experiment with a benthic lander bearing a multitude of sensors. The ML model uses wave parameters such as height, period and direction as input layers, which describe the ocean conditions, and strains in selected points of the lander structure as output layers. To streamline the dataset generation, a simplified approach was adopted, integrating analytical formulations based on Morison equations and numerical simulations through the Finite Element Method (FEM) of the designed lander. Subsequent validation involved Fluid–Structure Interaction (FSI) simulations, using a 2D Computational Fluid Dynamics (CFD)-based numerical wave tank of the entire ocean depth to access velocity profiles, and a restricted 3D CFD model incorporating the lander structure. A case study was conducted to empirically validate the simulated ML model, with the design and deployment of a benthic lander at 30 m depth. The lander was monitored using electrical and optical strain gauges. The strains measured during the testing period will provide empirical validation and may be used for extensive training of a more reliable model.

Keywords: fluid–structure interaction; benthic lander; structural health monitoring; machine learning models

check for updates

Academic Editors: Francesco De Vanna, Ernesto Benini and Hui Xu

Received: 22 October 2024
Revised: 12 December 2024
Accepted: 26 December 2024
Published: 7 January 2025

Citation: Santos, A.B.d.; Vasconcelos, H.M.; Domingues, T.M.R.M.; Sousa, P.J.S.C.P.; Dias, S.; Lopes, R.F.F.; Parente, M.L.P.; Tomé, M.; Cavadas, A.M.S.; Moreira, P.M.G.P. Predictive Analysis of Structural Damage in Submerged Structures: A Case Study Approach Using Machine Learning. *Fluids* **2025**, *10*, 10. https://doi.org/10.3390/fluids10010010

1. Introduction

Offshore structures play an important role in exploring and producing valuable energy resources from marine environments. The reliability and safety of these structures are of utmost importance and rely on the accurate prediction and assessment of potential structural damage due to ocean conditions. To address these challenges, Structural Health Monitoring (SHM) has emerged as a growing priority, combining sensor networks, advanced engineering materials, and computational knowledge systems, enabling engineers to evaluate the condition and performance of structures over time or estimate their remaining in-service life [1].

However, deploying sensor systems in submerged environments presents significant challenges related to durability, accessibility, and data reliability. The harsh underwater conditions can lead to issues such as corrosion, biofouling, and physical damage to sensors, compromising their longevity and performance. Additionally, the underwater environment poses obstacles to reliable data transmission, further complicating effective monitoring [2].

To overcome these physical limitations, virtual sensors have emerged as a transformative approach. These computational models leverage real-time data from a limited number of physical sensors, numerical simulation and machine learning techniques, to infer structural responses and conditions in areas where direct measurements are impractical or impossible. These tools enable comprehensive monitoring of critical regions of a structure while reducing the dependence on extensive physical sensor networks [3,4].

To support SHM efforts, empirical and numerical models have been used in coastal engineering, including sea level rise, hydrodynamics, and wave propagation [5]. These models incorporate complex, time-dependent interactions like wave-current and wave-structure dynamics, making them essential for generating data to develop SHM models. However, their computational intensity and inherent simplifications often limit their application for real-time monitoring. Recent advancements in machine learning (ML) are opening new developments in SHM applications to overcome these limitations, enabling more effective predictive maintenance and real-time damage detection. Although the amount of available data is increasing, the lack of sufficient and high-quality data is still a challenge, impacting the effectiveness and reliability of SHM systems. For instance, a recent study has applied deep learning techniques, such as a BRANN-based deterministic model for fragility assessment of deepwater drilling risers under storm conditions [6].

The SHM process consists of four key stages: load events sensing and determination of whether damage was imparted to the structure, identification of the precise loading location, evaluation of the extent and severity of the damage and, finally, prediction of the remaining life of the structure, taking the evaluated damage into account. This methodology is particularly useful for high-profile mechanical systems such as marine structures where performance is critical and on-site damage detection is challenging or even impossible [7].

To address these challenges and bridge the research gap in SHM for submerged structures and real-time monitoring, this study presents a methodology for predicting structural damage caused by ocean waves and currents. By combining wave parameters collected from an oceanic buoy with structural responses, the approach employs an ML model to deliver timely and reliable damage assessments. Acting as a virtual sensor, this model offers a new tool to improve real-time SHM in submerged environments.

This research is part of the Marewind Project, which aims to advance innovative solutions for offshore structures. Within this framework, and to address the challenges previously mentioned, a benthic lander was designed and manufactured to achieve three distinct objectives. The first two are related to testing materials: testing of antifouling coatings and testing new formulations for a concrete ballast system. The last goal, and the one that this paper is focused on, is the development of ML algorithms for predicting structural damage in submerged structures due to the inherent effects of ocean waves and currents. The data to train the Machine Learning models were initially generated using analytical and numerical methods. This process utilised historical data from a metocean buoy, provided by the Hydrographic Institute of Portugal, to model various sea states, characterised by wave parameters such as wave height, wave period and wave direction.

The subsequent sections detail the design of the benthic lander, the experimental apparatus and the methods developed to generate the data for training the machine learning models. A flowchart of the methodology is shown in Figure 1.

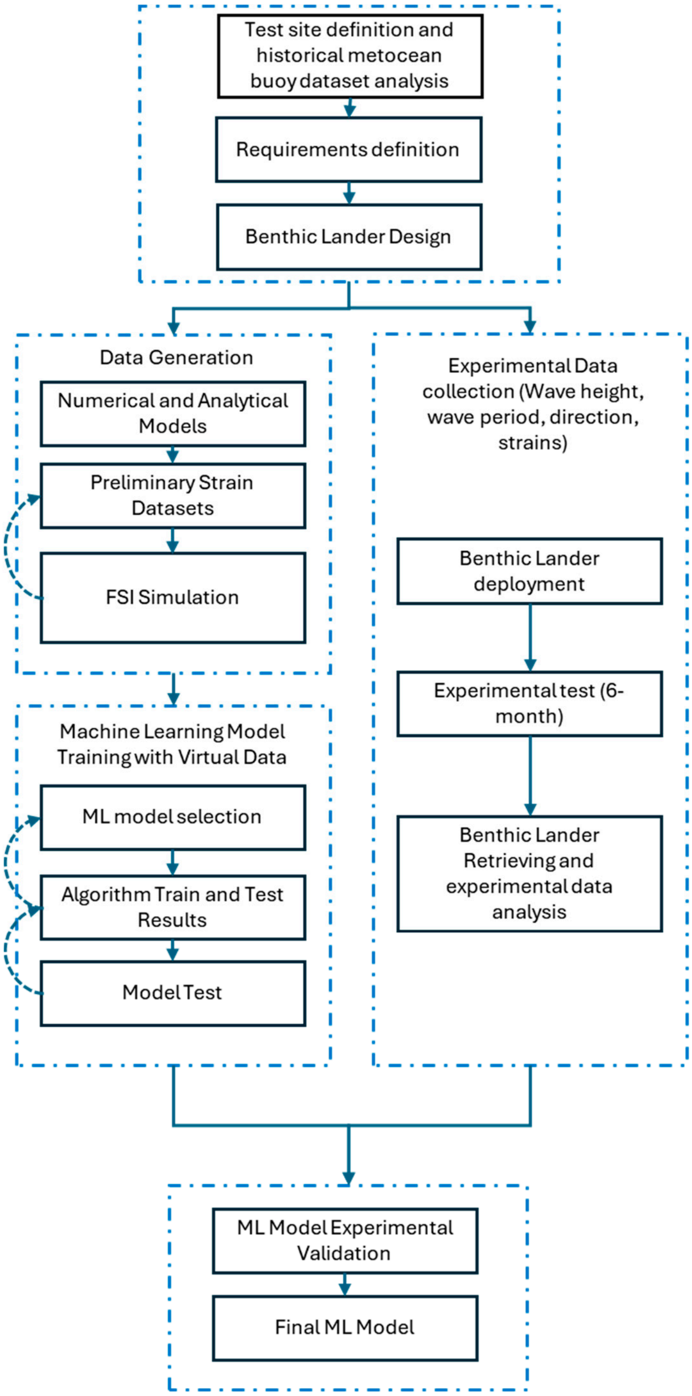

Figure 1. Schematic representation of the workflow.

2. Benthic Lander Design and Experimental Apparatus

The case study's test site is located near the Portuguese coastline, near Sines. A dataset with historical data from an oceanic buoy that is operating near the test site was acquired. This dataset comprises data about the ocean state, such as wave height and wave period, containing data from January 2017 to February 2024, with approximately 82,000 sea state measurements. This oceanic buoy is part of the Portugal Hydrographic Institute oceanic buoys network operating all over the Portuguese coastline. The historical dataset was analysed using wave theories such as the Airy Wave theory and the Stokes Wave theory [8]. The analysis supported the definition of the most critical scenario the lander could encounter, and generation of data for the machine learning models.

The selection of which wave theory to use was made according to the Le Méhauté diagram [9], which indicates the region of validity of different wave theories for various water depths and wave parameters.

The lander was deployed in the location illustrated in Figure 2. Simultaneously, a spotter buoy was anchored to the seabed at the same location. The spotter buoy measured the ocean states during the 6-month experiment, providing more accurate data regarding ocean conditions, and thus improving the reliability of the ML model.

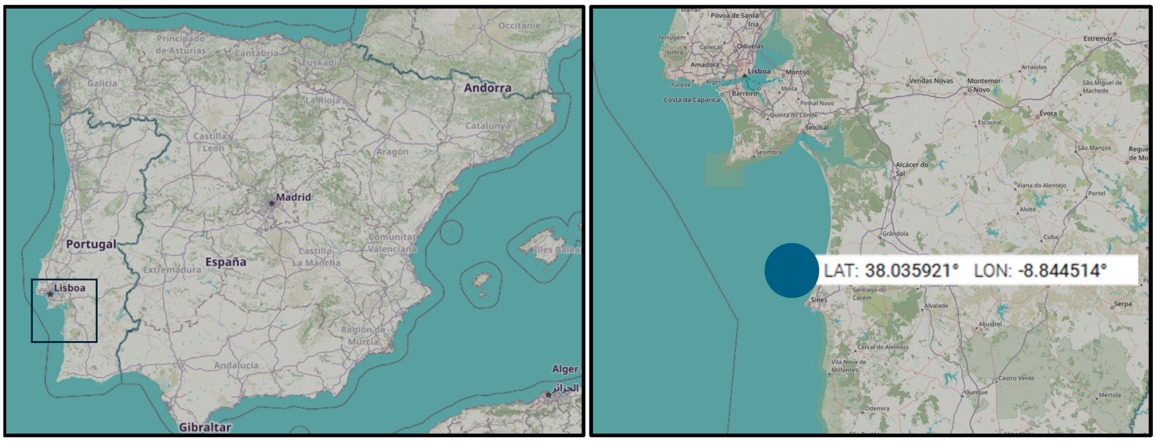

Figure 2. Lander deployment location. Adapted with permission from Ref. [10]. 2024, OpenStreetMap.

The lander is a welded structure of structural steel S275JR (EN 1.0044) treated with hot-dip galvanisation with a total mass of approximately 500 kg. The structure is tripod-shaped and was designed to be deployed into the benthic zone of the seabed at a 30 m depth. This design allows the assembly of steel plates on each leg, which increases the total weight of the structure, and the assembly of the electronic equipment in a central container. The lower centre of gravity and the high mass ensure the structure remains upright in challenging underwater conditions, including extreme currents and waves, allowing excellent stability on the ocean floor. The structure predominantly consists of circular tube profiles, except for the plates where the strain gauges are located.

The lander is monitored using two independent systems: a primary system comprising optical strain gauges, Fiber Bragg Grating (FBG) sensors and a secondary system of conventional electrical strain gauges. These sensors were mounted on four specific plates at the centre of the structure. Figure 3 shows the assembly process of the strain gauge sensors as well as the final structure.

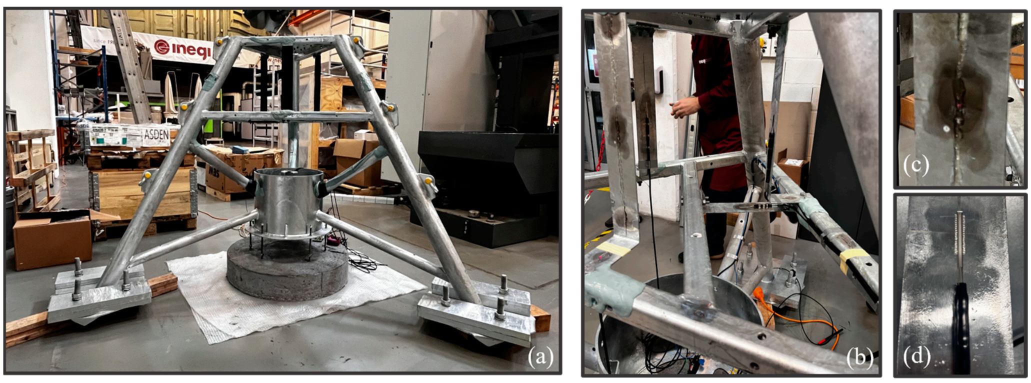

Figure 3. Final structure. (**a**) Overall lander structure; (**b**) specific plates mounted on the structure where strain gauges are mounted; (**c**) primary system—optical strain gauges' assembly; (**d**) secondary system—electrical strain gauges' assembly.

Two critical scenarios were identified to guarantee the success of the experiment. The first scenario addressed the stages of deploying the structure in the ocean and retrieving it. In this phase, the primary considerations were the total weight of the structure along with any mounted equipment, which together pose the most significant challenge for the deployment operation. The second scenario focused on the impact of ocean currents and waves on the structure, due to the pressures exerted by different sea states. For each scenario, a Finite Element Model (FEM) of the lander was developed.

While the load calculation was straightforward in the first scenario, the second scenario required a more detailed analysis with the calculation of the loads for each individual component. Figure 4 illustrates the adopted sub-division.

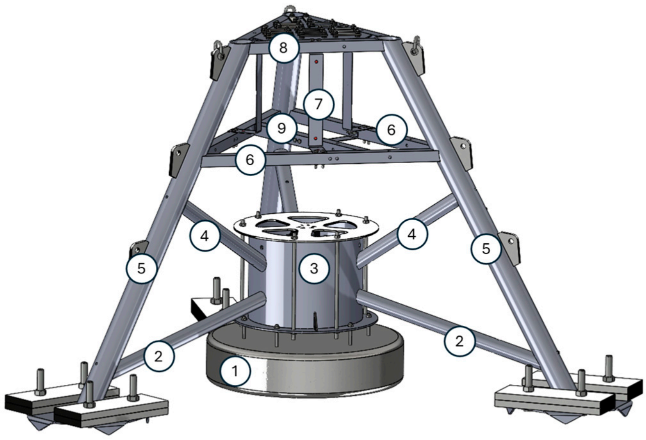

Figure 4. Division of lander structure into subsections for load calculation.

As a widely used method for wave loading prediction, Morison's Equation was employed to calculate the loads suffered by each component of the lander. It comprises two main components: the inertial force (F_I), and the drag force (F_D) [11].

$$F = F_D + F_I, \tag{1}$$

$$F = 0.5\rho C_D |v| v A_p + C_M \rho V_{vol} \dot{v}, \tag{2}$$

where ρ is the density, v is the fluid velocity, A_p is the projected area of the structure perpendicular to the flow and V_{vol} is the displaced volume.

The values of the drag (C_D) and inertia (C_M) coefficients are typically determined experimentally, being a function of the Reynolds number (Re), the Keulegan–Carpenter number (KC) and the roughness (Δr). The recommended practical coefficient values for the coefficients were assumed considering each part's geometry and its Reynolds number [12].

The critical ocean condition identified on the historical dataset is outlined in Table 1. However, to ensure the structural integrity of the entire experimental test, a safe approach was adopted, and a 5 m/s velocity magnitude was considered for the numerical simulation.

Table 1. Wave parameters for the selected ocean state.

Wave Period	Wave Height	Wavelength	Depth
9.39 s	6.73 m	105 m	30 m

Results and Discussion

Figure 5 shows the results obtained in the numerical simulation, validating the structure design.

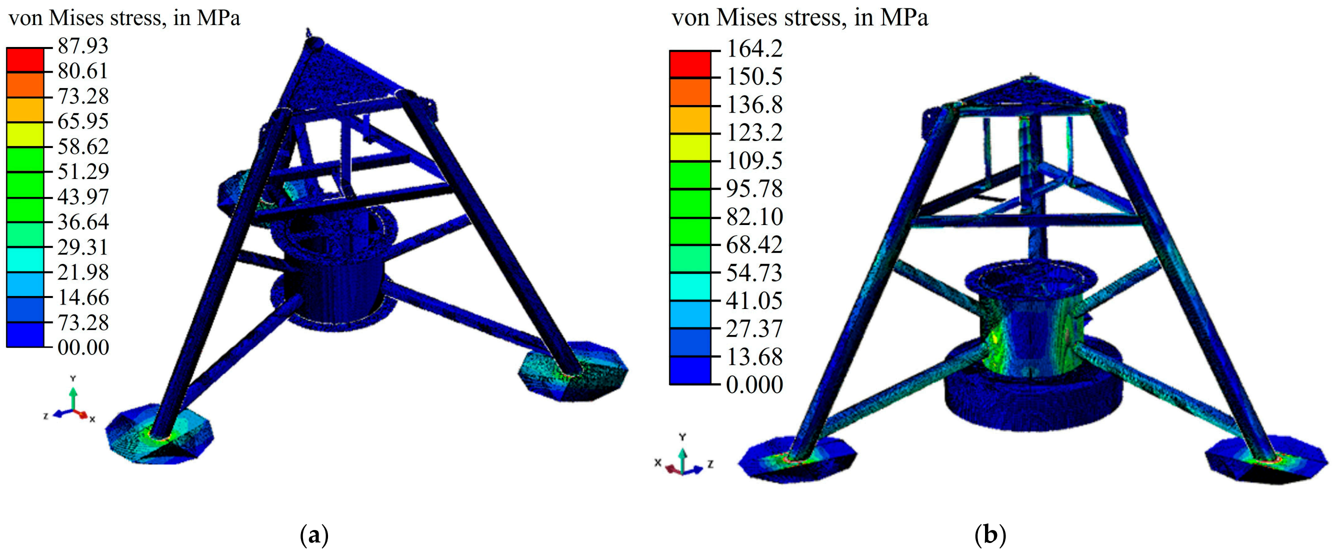

Figure 5. FEA results; (**a**) first scenario: structure hanging—max von Mises stress 88 MPa located on the leg base of the lander; (**b**) second scenario: structure deployment—max von Mises stress of 164 MPa located on the round tube at the centre of the lander.

The analysis showed that the highest calculated von Mises stress is located at the base of the structure and the tube in the centre, for the first and second scenarios, respectively. These results were compared with the material properties (yield stress of 275 MPa) to ensure that the lander can withstand the demands in each scenario.

3. FSI Methodology

Physical modelling of a structure subjected to hydrodynamic loads is usually performed via a two-stage procedure: a CFD simulation followed by an FEM analysis.

The approach for Fluid–Structure Interaction (FSI) simulations combines the Finite Volume Method (FVM) with the volume of fluid (VOF) method to create the CFD models. For these analyses, the commercial software Ansys Fluent was used. In the CFD models, pressure fields on the lander structure were calculated and then applied to a Finite Element Method (FEM) model to assess structural responses to hydrodynamic wave loads. For the FEM analysis, the commercial software Ansys Mechanical was used.

Considering the extension of the problem, the main challenge in designing the CFD numerical model was to create an accurate simulation with reduced computational cost. To meet these goals, the CFD model was split into two parts. This method lowered the computing effort needed, avoiding an entire ocean-depth 3D CFD model of the test site.

The first part of the approach focused on a fully developed 2D domain, with a depth corresponding to the full scale of the test site's bathymetry and a length sufficient to characterise the wavy flow while minimising undesirable numerical effects. For this purpose, a numerical wave tank was developed. The primary objective was to generate velocity profiles at each time step that accurately reflected the impact of surface waves at the bottom of the domain.

The velocity profiles, generated in a 2D numerical wave tank, were applied as inlet boundary conditions to a 3D model that incorporates the lander structure. This approach significantly reduced computational cost, as the 3D domain could be limited in size and considered fully submerged, eliminating the need for the computationally intensive VOF multiphase model. The 3D CFD model, restricted to this configuration, produces pressure fields that are subsequently used in the structural analysis of the lander within a one-way FSI framework.

3.1. Two-Dimensional Numerical Wave Tank: Velocity Profile Generation

The configuration of the numerical wave tank model is organised into three primary stages: (1) the geometry setup, where the physical dimensions of the model domain are defined; (2) the mesh generation, in which the computational grid is created and refined near the still water level (SWL) to capture the free surface dynamics accurately; and (3) the wave and physics setup, which involves specifying the type of analysis, domain properties, wave generation and other parameters related to air–water interactions. The surface tension at the air–water interface is considered negligible. The air temperature is set to 25 °C, corresponding to a density of 1.185 kg/m^3. The fluid temperature is also set to 25 °C, with a density of 1030 kg/m^3 to represent saltwater conditions.

3.1.1. Governing Equations

The solver in ANSYS Fluent 2023 is based on the finite volume method (ANSYS Inc., Canonsburg, PA, USA, 2023). This method divides the computational domain into a series of control volumes and discretises the governing equations, enabling iterative solutions over each control volume. Through this process, approximate values of the flow variables are computed at discrete points across the domain. The governing equations are the continuity equation for constant density and the Navier—Stokes equations for an incompressible, constant viscosity fluid, given by [13]:

$$|\nabla| \cdot \vec{u} = 0, \tag{3}$$

$$\frac{\partial \cdot \vec{u}}{\partial t} = -\vec{u} \cdot I\vec{u} + \frac{1}{\rho Re}\nabla \cdot \left[(\mu + Re\mu_t)\left(\nabla\vec{u} + \left(\nabla\vec{u}\right)^T\right)\right] - \frac{\nabla P}{\rho} + \frac{\vec{a}}{F_r}, \tag{4}$$

where $\vec{u}$, P, ρ, μ, μ_t $\vec{a}$ and F_r are the non-dimensional velocity, pressure, density, dynamic viscosity and dynamic turbulent/eddy viscosity fields, gravitational acceleration and Froude number, respectively.

The volume of fluid (VOF) method is employed to track the free surface position. This method calculates the volume fraction of each fluid, present within each control volume. The volume fraction is determined using the following equation:

$$\frac{\partial \alpha}{\partial t} + \nabla\left(\alpha\vec{V}\right) = 0, \tag{5}$$

where $\vec{V}$ represents the velocity vector, and α denotes the water volume fraction. The mixture density is calculated based on the volume fraction using the following equation:

$$\rho = \alpha\rho_\omega + (1-\alpha)\rho_a, \tag{6}$$

where ρ_ω represents the water density and ρ_a the air density.

3.1.2. Geometry and Boundary Conditions

The geometry domain and location of boundary conditions used in the 2D simulations can be seen in Figure 6, where it is important to highlight the presence of refinement zones near the water–air interface and inflation near the wall (bottom of the sea) to control parameters related to the turbulence model (κ-ω SST) and keep y^+ close to unity.

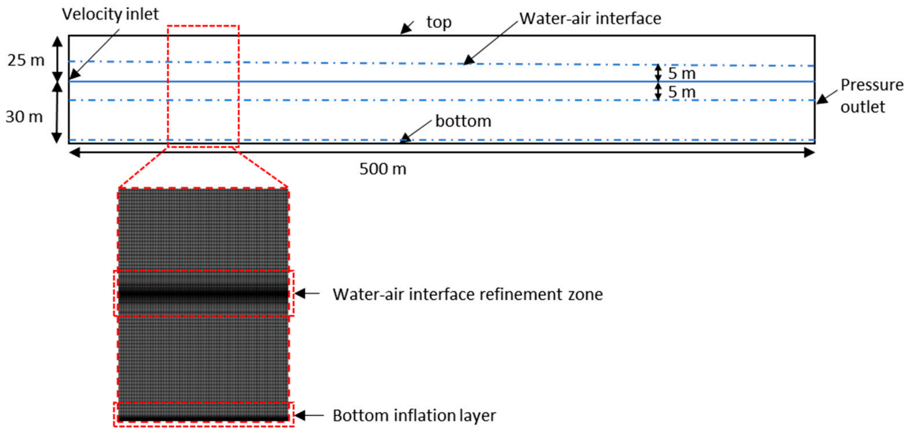

Figure 6. Numerical wave tank geometry and mesh refinement zones.

An inlet velocity method was applied to the model. A pressure outlet boundary condition was implemented at the far field boundary for wave absorption. Similar to the approaches used by Kim et al. [14], a damping zone featuring a numerical beach was established near the far field boundary to dissipate wave energy and minimise reflections within the simulation domain.

ANSYS Fluent code offers a static boundary method in the open channel flow and open channel wave boundary condition volume of fluid sub-models. The generation of incoming waves was achieved by defining a velocity inlet boundary condition coupled with an open channel wave boundary condition. This boundary method enabled the generation of the regular waves.

3.1.3. Simulation Parameters

Simulations were carried out using a transient approach. Within each time step, a minimum residual of 10^{-4} was imposed. Temporal discretisation is crucial for the quality of the solution in computational simulations. Large time step intervals can lead to wave damping, while small intervals significantly extend the computational time required to reach a solution. Therefore, it is essential to select the time step interval carefully.

Multiple studies have proposed recommended values for the optimal time step interval. Marques Machado et al. [15] concluded that the optimal time step is reached by dividing the wave period by 50 intervals (T/50). This conclusion aligns with the recommendation from another work [16] that suggests a maximum interval of T/40. However, other researchers [17,18] have suggested using even smaller time step values, recommending intervals equal to or less than T/100. A time step interval of T/100 was chosen for all the sea states.

A summary of the numerical parameters used in the setup for the 2D numerical wave tank can be found in Table 2.

Table 2. Simulation setup parameters for the numerical wave tank.

Parameter	Value
Solver	Pressure-based
Time Formulation	Transient
Turbulence model	$\kappa - \omega$ SST
Scheme	PISO
Multiphase model	VOF
Time step (s)	T/100
Number of time steps	10 Wave Period
Max. iterations per time step	100

3.1.4. Computational Mesh

A multizone method was used to create a structured mesh, in which the domain is divided into quadrilateral elements. A central zone with a finer mesh was established to improve the resolution of steep gradients at the water–air interface (refer to Figure 6). This refinement was accomplished using the edge sizing feature, allowing for increased divisions within the targeted area.

The computational mesh was optimised taking into consideration both the highest wavelength and wave height found in the metocean dataset. Various criteria have been proposed to determine the appropriate mesh size for simulations. Among these, Havn [18] suggests several criteria, which are summarized in Table 3.

Table 3. Grid size parameters for mesh refinement in the numerical wave tank.

Parameter	Value
Cells per wavelength	$\frac{\lambda}{\Delta x} > 100$
Cells per wave amplitude	$\frac{a}{\Delta z} > 10$
Aspect Ratio	$\frac{\Delta x}{\Delta z} < 10$

Three different meshes were created to evaluate the influence of mesh dimensions on the study's results, and they are described in Table 4. These meshes follow the recommendations suggested by Haven [18]. Apart from differences in their dimensions, all the constructed grids share qualitative features similar to those shown in Figure 6.

Table 4. Grid parameters for different mesh configurations in the numerical wave tank.

Mesh ID	Number of Divisions	Δx [m]	$\frac{\lambda}{\Delta x}$	Number of Division Interface z	Δz [m]	$\frac{a}{\Delta z}$
1	525	0.952	131.3	25	0.4	8.41
2	800	0.625	200.08	31	0.322	10.45
3	1200	0.417	299.89	50	0.2	16.825

Number of Divisions represents the total number of grid cells along the x-direction. Δx [m] is the grid spacing in the x-direction, and $\lambda/\Delta x$ indicates the ratio of wavelength to grid spacing, reflecting the resolution for capturing wave propagation. Number of Division Interface z refers to the number of grid cells along the z-direction at the water–air interface. Δz [m] is the grid spacing in the z-direction, and $a/\Delta z$ denotes the ratio of wave amplitude to grid spacing, which determines the accuracy of wave height representation.

The numerical results are validated by comparing the surface elevation of the waves, generated within the numerical wave tank, against the theoretical profiles derived from Stokes' second-order wave theory. The analysis focuses on specific locations within the tank, namely at $x = \lambda$ and $x = 2\lambda$, where λ represents the wavelength.

The results from three different mesh resolutions are compared in Figures 7 and 8, revealing that the surface elevations across all meshes are similar. The discrepancies observed between the numerically simulated and theoretically predicted surface elevations can be attributed to some factors inherent to the numerical modelling of wave dynamics. One notable factor is the interaction of waves with the tank boundaries, particularly given the significant ratio of the wavelength to the tank length of the wave simulated.

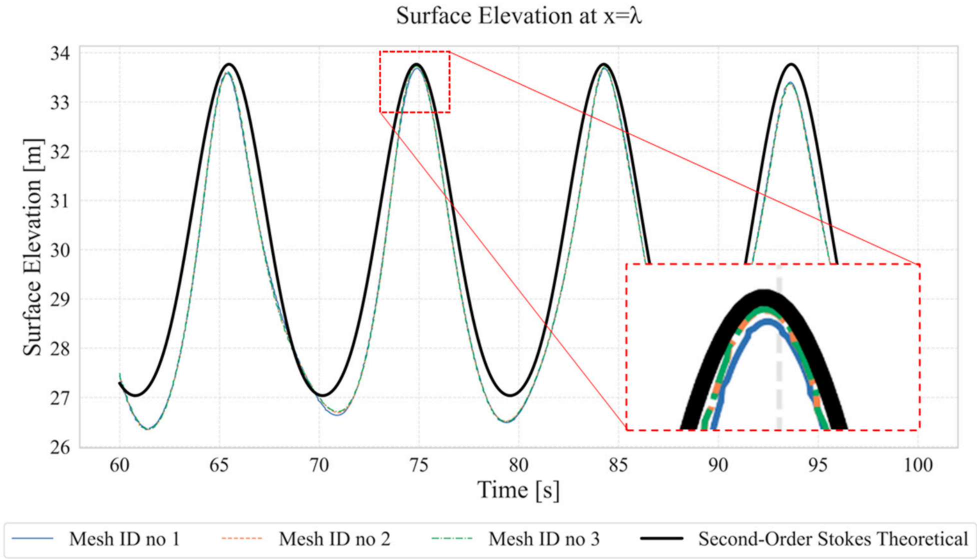

Figure 7. Free surface elevation comparison between numerical and theoretical wave at x = λ.

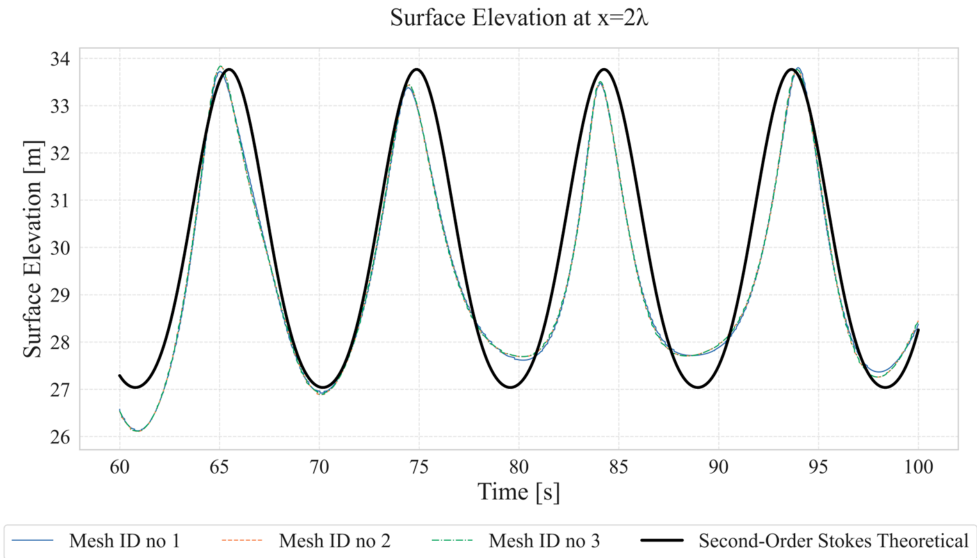

Figure 8. Free surface elevation comparison between numerical and theoretical wave at x = 2 λ.

3.2. Three-Dimensional Hydrodynamic Model: Pressure Distribution and FSI

The velocity profiles obtained in the previous numerical wave tank are used to set the velocity inlet for the 3D restricted domain. This restricted domain reduced the computational cost. The 3D domain has a limited dimension and is totally submerged, without the need for the high-demanding VOF multiphase model.

3.2.1. Computational Domain and Boundary Conditions

A computational domain with the shape of a cube that encloses the lander structure was created. The dimensions of the domain are 5 × 5 × 5 m (in width × depth × height). An inlet boundary condition was applied to two faces and a pressure outlet was applied to the other two faces of the domain. A symmetry boundary condition was applied on top, and a wall boundary condition was applied to the bottom. The boundary conditions and the spatial arrangement of the lander structure within the 3D computational domain are represented in Figure 9.

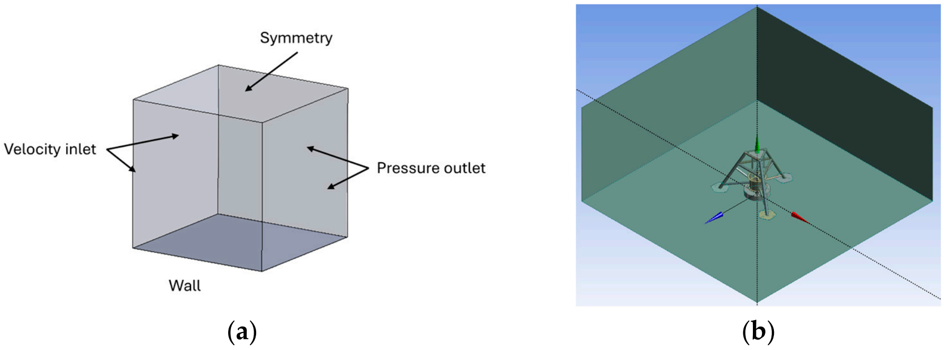

Figure 9. Three-dimensional computational domain layout. (**a**) Applied boundary conditions, (**b**) lander structure placed at the centre of the domain.

3.2.2. Grid Generation and Grid Independence Study

Grids for the CFD domain were created using the Poly-Hexcore Mosaic meshing technology developed by ANSYS. Mosaic meshing in Ansys Fluent improves CFD simulations by combining various mesh types to optimise both mesh quality and computational efficiency. It integrates poly-hexcore meshes in the bulk region with high-quality layered poly-prism meshes near boundaries, thereby reducing cell count and increasing solver speed [19–21].

In Figure 10, the implementation of Mosaic technology in the 3D mesh generation of the domain near the lander structure is shown, demonstrating the use of octree hexahedral elements within the bulk region (a), isotropic poly-prisms in the boundary layer (b) and mosaic polyhedral elements facilitating the transition between these zones (c).

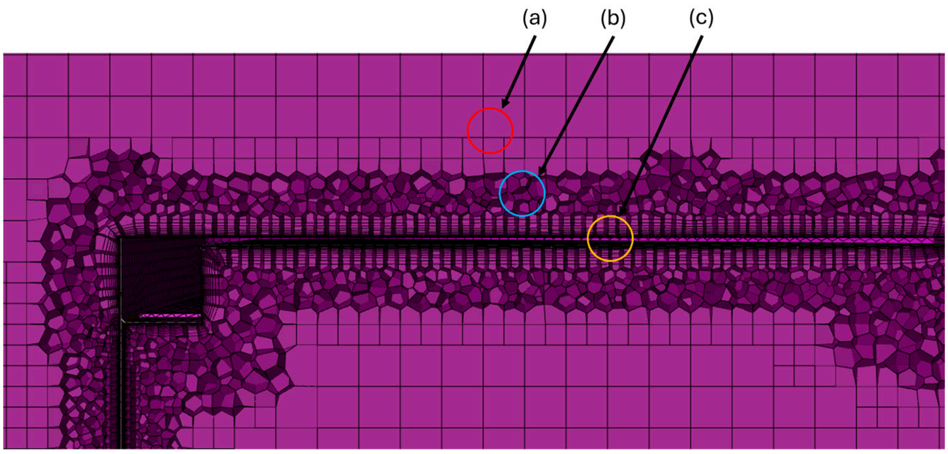

Figure 10. Mesh refinement in the vicinity of the interfaces. (**a**) Octree hexahedral elements used for bulk meshing; (**b**) isotropic poly-prism elements applied near wall boundaries for accurate boundary layer resolution; (**c**) mosaic polyhedral elements employed for efficient and smooth transition between regions, optimising both accuracy and computational cost in the simulation.

The complexity of the geometry posed a challenge to the generation of a fully structured mesh. Local size controls were applied within bodies of influence to achieve a finer mesh around the lander structure. Figure 11 demonstrates how the body of influence enables a seamless transition from the coarser mesh in the outer domain to the finer mesh near the lander structure.

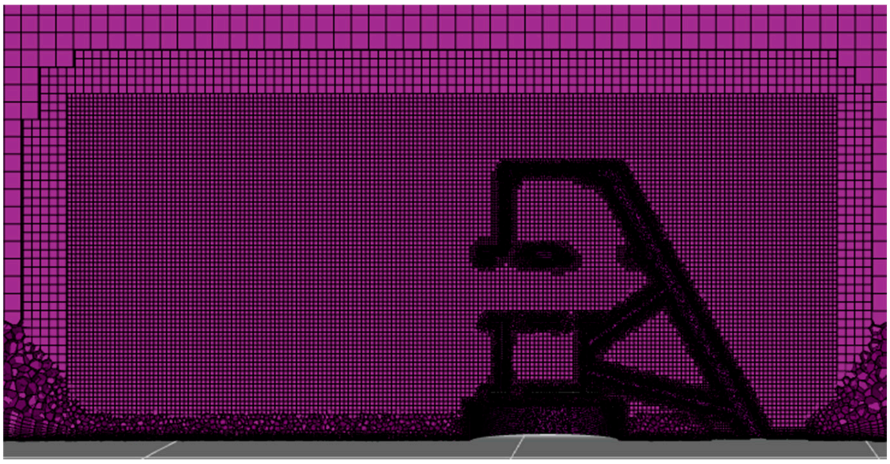

Figure 11. Application of a body of influence for mesh refinement.

The resultant pressure and velocity values from the CFD simulations serve as input parameters of the structural study, which implies that the CFD results are required to be accurate. With this in mind, a study regarding grid convergence was performed. The parameter used for the analysis was the drag force on the direction of the flow.

Five meshes with different degrees of refinement were created. Table 5 shows the drag force versus the number of elements for each created different mesh. The variation parameter regarding the most refined mesh $\varepsilon_i = \frac{\overline{P}_{coarser} - \overline{P}_{finer}}{\overline{P}_{finest}}$ was calculated and is shown in Table 5. The drag force was measured after 12 s of simulation.

Table 5. Different meshes created and results of mesh independence study.

Mesh ID	Number of Cells	Drag Force [N]	ε_i (%)
1	2,104,970	112.4	−9.36
2	4,436,569	125.2	−8.05
3	5,207,808	136.2	−0.29
4	5,511,176	136.6	−0.07
5	8,424,436	136.7	-

A relative difference in drag force of 0.29% between mesh number 3 and mesh number 4 and 0.07% between mesh number 4 and mesh number 5 was detected. Therefore, mesh number 4, comprising 5,511,176 cells, was chosen, supporting the flow dynamics simulation around the lander without the excessive computational demand of mesh number 5.

Mesh number 4 incorporates a body of influence with a target mesh size of 17 mm. Local sizing at the lander surface was adjusted to a maximum face size of 4 mm, and a boundary layer with 10 layers and a growth rate of 1.2 was added to capture detailed flow characteristics. A maximum skewness of 0.85 and an average skewness of 0.03 were obtained, as well as a minimum orthogonal quality of 0.15 and an average of 0.96.

3.2.3. Simulation Parameters

The turbulence model was the $\kappa - \omega$ method, with enhanced wall function. A mesh of about five million elements was used in all simulations. The time step used in the 3D model had to match the one selected in the numerical wave tank simulation for the corresponding wave under analysis. A summary of the numerical parameters used in the setup for the 3D simulations can be found in Table 6.

Table 6. Simulation setup parameters for the 3D domain simulations.

Parameter	Value
Solver	Pressure-based
Time Formulation	Transient
Turbulence model	$\kappa - \omega$ SST
Scheme	SIMPLE
Time Step (s)	T/100
Number of Time Steps	10 Wave Period
Max. Iterations per Time Step	100

The hydrodynamic analysis conducted via CFD produced pressure fields as the primary outputs. These pressure fields were subsequently applied to the structural model in a one-way FSI framework, serving as boundary conditions for the FEM simulation to evaluate the structural response to hydrodynamic loads. Figure 12 illustrates the pressure field imported from the CFD analysis, which is applied to the structural model for further analysis.

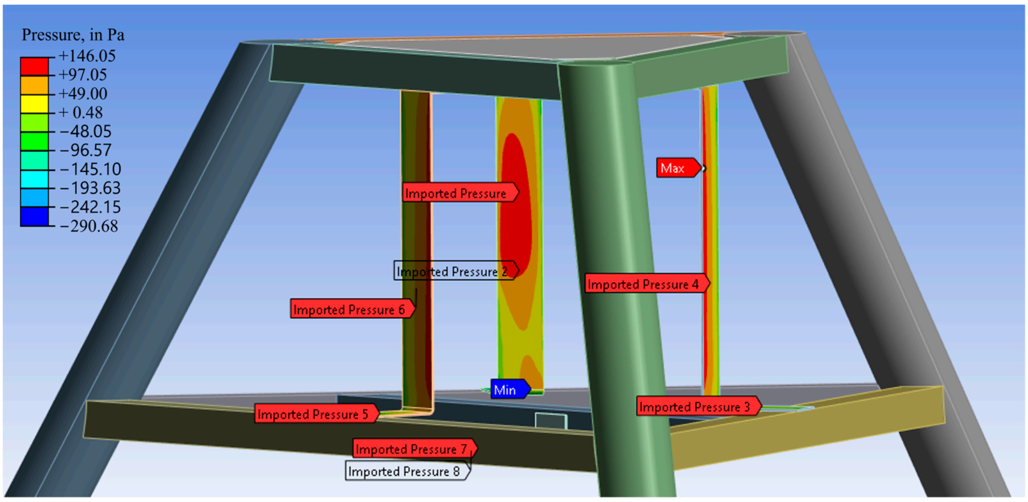

Figure 12. Imported pressure from the CFD analysis.

4. Preliminary Dataset Generation

To address the limitations posed by time-consuming FSI simulations, an alternative approach and a preliminary dataset of strains were created to generate enough data to develop and select the ML models. One major issue is ensuring data quality, as poor-quality data can lead to inaccurate or misleading model predictions [22].

The adopted approach uses a Finite Element Model of the structure to calculate the strains. Similar to the design validation, the loads to apply on the FEM model were calculated with the Morison equations. Figure 13 displays the locations where strain measurements were taken, highlighting the four dedicated plates and the specific points selected for strain calculations.

The approach computes the load for each sea state in the historical wave dataset using wave theories and the Morison equation. Water particle velocities were calculated at a height of one meter, corresponding to the strain gauge installation height. A steady current velocity of 0.5 m/s was included to account for ocean currents. The loads on each plate were computed using the Morison equation, with drag and added mass coefficients obtained from DNV-RP-C205 (Appendices E and D, respectively), which are suitable for thin plates perpendicular to the flow.

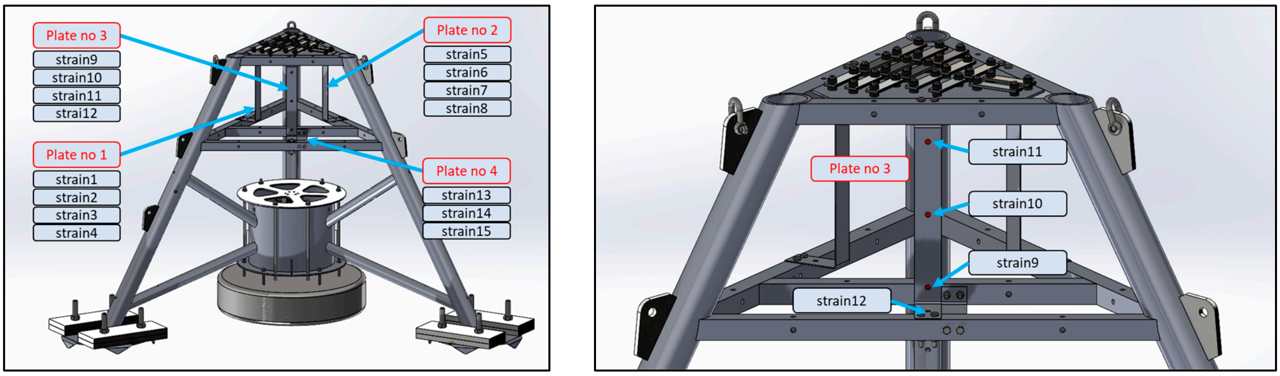

(**a**) (**b**)

Figure 13. Strain gauges' position on the lander structure; (**a**) general strain gauge position overview and plate identification; (**b**) detailed view of the strain gauges' positions for plate No 4.

Strain computations were then performed using a Finite Element Model (FEM) of the structure. Figure 14 illustrates the application of the loads on the dedicated plates, as well as the discretisation of the plates into finite elements for the structural analysis.

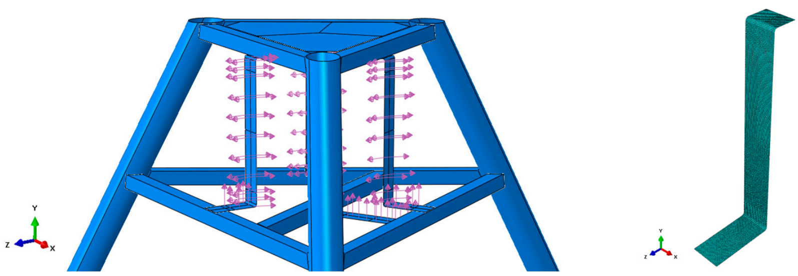

(**a**) (**b**)

Figure 14. Lander structure load and mesh details; (**a**) representation of the loads applied to the FEM model; (**b**) a general overview of the mesh used in the FEM simulations of a dedicated plate.

The resulting dataset includes strain values calculated at 15 points across four plates, corresponding to the locations where strain gauges were installed on the lander structure in the experimental study. Figure 15 shows the strains calculated at location 2 on plate 1 as a representative example.

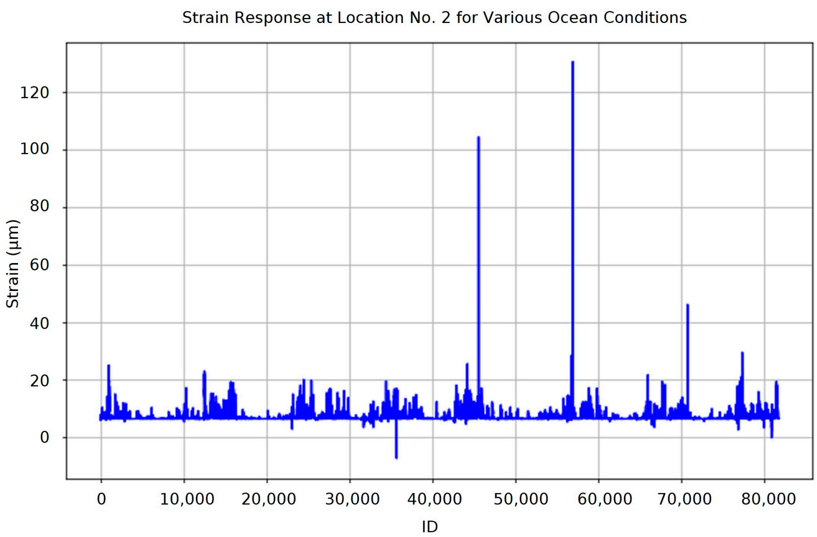

Figure 15. Strain response for all ocean conditions at location no. 2 on plate no. 1.

Strains were calculated for cases involving only the current effect and for the selected sea state, as shown in Tables 7 and 8. These results were compared with those derived from preliminary datasets using the FEM results. While the magnitudes differed, a correlation in strain behaviour was observed across both approaches. Specifically, both methods consistently identified high- and low-strain areas across the plates. Moreover, agreement was found in detecting compressive and tensile states along the vertical plates. However, this correlation did not extend to the horizontal plate, where the analytical and FEM methods failed to capture the expected strain behaviour.

Table 7. Strain comparison resulting from current effect.

Plate Number	Location ID	Preliminary Dataset Results	FSI Results
Plate 1	STRAIN 1	−4.1188	−4.9787
	STRAIN 2	6.1024	7.1612
	STRAIN 3	−5.7090	−7.2144
	STRAIN 4	1.5425	2.1410
Plate 2	STRAIN 5	2.0614	3.1670
	STRAIN 6	−3.0528	−4.6700
	STRAIN 7	2.8567	4.7764
	STRAIN 8	−0.7763	−1.2090
Plate 3	STRAIN 9	2.0603	2.7780
	STRAIN 10	−3.0485	−4.1100
	STRAIN 11	2.8517	4.2820
	STRAIN 12	−0.7830	−1.1960
Plate 4	STRAIN 13	−0.0156	0.1867
	STRAIN 14	−0.0084	−0.5300
	STRAIN 15	−0.0027	0.2605

Table 8. Strain comparison resulting from the selected ocean state.

Plate Number	Location ID	Preliminary Dataset Results	FSI Results
Plate 1	STRAIN 1	−13.6271	−52.478
	STRAIN 2	20.1919	75.074
	STRAIN 3	−18.8938	−77.058
	STRAIN 4	5.1253	24.583
Plate 2	STRAIN 5	25.3005	71.284
	STRAIN 6	−37.5133	−103.94
	STRAIN 7	35.0922	103.57
	STRAIN 8	−9.4765	−28.712
Plate 3	STRAIN 9	−11.6953	−47.745
	STRAIN 10	17.3130	70.118
	STRAIN 11	−16.1931	−71.221
	STRAIN 12	4.4529	17.861
Plate 4	STRAIN 13	0.0983	1.821
	STRAIN 14	0.0195	−1.020
	STRAIN 15	0.0314	1.403

5. AI Predictive Models

The machine learning algorithms developed for the prediction of forces to which the lander is subjected to are presented in this chapter.

In this study, various machine learning algorithms were evaluated to identify the most effective models for predicting structural damage based on wave parameters and strain data. Among the models tested, particular emphasis was placed on the Artificial

Neural Network Multilayer Perceptron (ANN MLP) and random forest algorithms due to their demonstrated proficiency in handling the complex and nonlinear data patterns of the strains and wave dataset. The ANN MLP is renowned for its ability to model intricate relationships through multiple layers of interconnected neurons, while the random forest algorithm excels in ensemble learning by constructing a multitude of decision trees for robust predictions [23,24].

The methodologies employed for data preprocessing, model training, validation and evaluation are detailed in the subsequent sections, providing a comprehensive overview of our analytical approach.

5.1. Dataset Description

The dataset consists of 81,724 samples. Each sample is composed of three inputs, namely Wave Height (WS_30) [m], Wave Period (THS_30) [s] and Direction (WAVE_THTP) [°]; and fifteen outputs corresponding to the fifteen different strains calculated along the lander. This way, an 81,724 $\times$ 18 matrix has been imported for machine learning development.

A Pearson correlation analysis was conducted, resulting in the correlation matrix shown in Figure 16. This matrix provides insight into the linear relationship between pairs of variables. Each value represents the degree of correlation between two variables, ranging from -1 to 1. A value of -1 indicates a perfect inverse correlation, 1 indicates a perfect direct correlation, and 0 signifies no linear relationship. Along the diagonal, where each variable is compared to itself, the correlation is always 1.

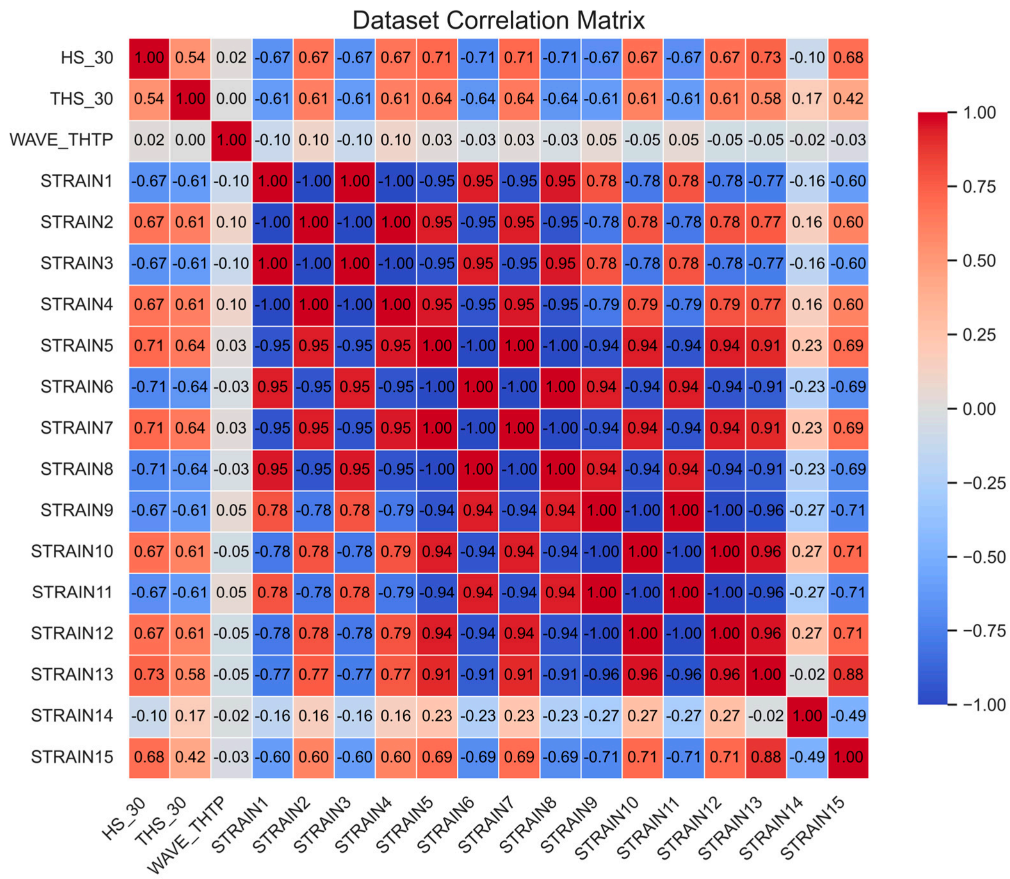

Figure 16. Pearson's correlation matrix.

Variables with an inverse correlation are marked in blue, while those with a direct correlation are shown in red. The analysis reveals that 9 out of 15 outputs exhibit full relation with other variables. For instance, strain 1 is inversely correlated with strain 2 and strain 4 but directly correlated with strain 3. Similarly, strain 5 and strain 9 are inversely correlated with strain 6 and strain 8, and strain 10 and strain 12, respectively, while being directly correlated with strain 7 and strain 11. These correlations have a physical basis, as illustrated in Figure 16. Each correlation group corresponds to one of the three plates depicted in Figure 13.

To analyse data distribution, the mean, standard deviation, minimum and maximum values, number of zeros and 25, 50, and 75 percentiles of all the variables have been computed. The data, shown in Table 9, indicate that for all variables, most of the measurements are close to the mean value of that variable while standard deviation and min/max values are considerably far away from that mean. That suggests that the sample behaves as a normal distribution, which has the majority of the samples next to the mean value and then the frequency of the data is reduced as it goes further from this value. This is coherent as the pattern of the inputs is replicated in the outputs. It can also be observed that the number of zeros in the outputs is null

Table 9. Statistical analysis of the strain and wave dataset.

Validation Set	Wave Height	Wave Period	Wave Direction	Strain 1	Strain 2
Mean	1.6695	6.7941	299.3296	−4.6397	6.8742
Std	0.8126	1.8251	22.9865	1.1155	1.6532
Min	0.2600	2.8000	1.0000	−87.9362	−7.6519
25%	1.0600	5.4000	293.0000	−4.6710	6.1025
50%	1.5200	6.6000	304.0000	−4.1736	6.1835
75%	2.1000	8.0000	311.0000	−4.1190	6.9199
Max	14.1500	18.6800	359.0000	5.1527	130.3429

5.2. Data Pre-Treatment

The dataset was divided into training (70%), validation (15%) and test (15%) sets using a binning process to ensure that each subset accurately represented the overall data distribution. This stratified division is essential for maintaining the statistical properties across all subsets, thereby improving the models' ability to generalise to new, unseen data. A visual representation of this dataset division is provided in Figure 17, while the statistical parameters for the training, testing and validation datasets are detailed in Tables 10–12, respectively.

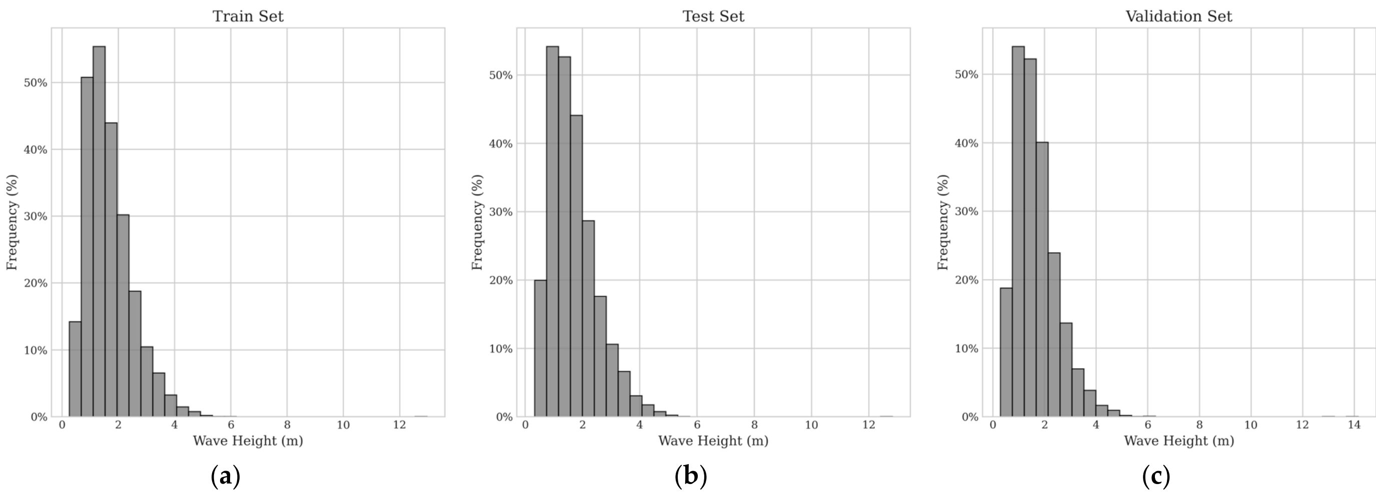

Figure 17. Histograms of the data splits for machine learning model development. (**a**) Training dataset, (**b**) testing dataset and (**c**) validation dataset.

Table 10. Statistical parameters for the training dataset.

Train Set	Wave Height (m)	Wave Period (s)	Wave Direction (°)
Mean	1.669	6.794	299.384
Std	0.811	1.823	28.862
Min	0.260	2.800	1.000
25%	1.060	5.400	293.000
50%	1.520	6.600	304.000
75%	2.100	8.000	311.000
Max	12.970	18.680	359.000
Count		57,206	

Table 11. Statistical parameters for the testing dataset.

Test Set	Wave Height (m)	Wave Period (s)	Wave Direction (°)
Mean	1.669	6.798	299.228
Std	0.817	1.833	22.149
Min	0.290	3.000	1.000
25%	1.060	5.400	293.000
50%	1.520	6.600	302.000
75%	2.100	8.000	311.000
Max	14.150	18.680	359.000
Count		12,259	

Table 12. Statistical parameters for the validation dataset.

Validation Set	Wave Height (m)	Wave Period (s)	Wave Direction (°)
Mean	1.669	6.798	299.227
Std	0.817	1.833	22.149
Min	0.290	3.000	1.000
25%	1.060	5.400	293.000
50%	1.520	6.600	302.000
75%	2.100	8.000	311.000
Max	14.150	13.000	359.000
Count		12,259	

Prior to executing the predictive algorithms, data normalisation was performed to reduce disparities in scale among the features. Normalisation is crucial because it adjusts the scales of input features, preventing variables with larger magnitudes from unduly influencing the model outcomes. This is especially important for algorithms like ANNs which are sensitive to the scale of input data due to the optimisation processes they employ [25].

Standard scaling was applied to the training dataset wave height and period, and the obtained scaling mechanism was then used on the test and validation sets. Standard scaling transforms features to have a mean of zero and a standard deviation of one. This transformation is beneficial for algorithms that assume data are normally distributed, helping improve model performance and stability [26]. The wave direction was split into sine and cosine components, ensuring their values range from -1 to 1, which helps maintain directional continuity and improves model input consistency.

5.3. Models

5.3.1. Random Forest Regressor

The Random forest algorithm (RFR) is an ensemble learning method that constructs multiple decision trees during training and outputs their aggregated prediction for regression tasks. This model enhances predictive accuracy and controls overfitting by leveraging the diversity of individual trees.

To optimise the performance of the RFR model, four hyperparameters were tuned:

- Number of Estimators: This parameter determines the number of decision trees in the forest. Increasing the number of estimators generally improves model performance by reducing variance but also increases computational cost.
- Maximum Tree Depth: Controlling the depth of the individual trees helps prevent overfitting by limiting the complexity of the model. Shallower trees reduce the risk of capturing noise in the data.
- Maximum Features: This parameter sets the number of features to consider when looking for the best split at each node. Introducing randomness in feature selection enhances model generalisation by reducing correlation among trees.
- Minimum Number of Samples Required to Split an Internal Node: This hyperparameter specifies the minimum number of samples needed to split an internal node. Increasing this value can prevent the model from capturing noise, thereby reducing overfitting and decreasing computational effort.

A grid search combined with cross-validation was employed to identify the optimal hyperparameter values.

The hyperparameter tuning process identified the optimal values, which are presented in Table 13.

Table 13. Hyperparameters' best-fit value for random forest regressor algorithm.

Hyperparameter	Best-Fit Value
Number of estimators	1000
Minimum samples split	2
Maximum features	1.0

The performance of the RFR model was evaluated on the test dataset. The following evaluation metrics were used [27]:

- Mean Squared Error (MSE): measures the average squared difference between the predicted and actual strain values.

$$\mathrm{MSE} = \frac{1}{n}\sum_{i=1}^{n}(y_i - \hat{y}_i)^2 \tag{7}$$

- Root Mean Squared Error (RMSE): provides the error magnitude in the same units as the output variable.

$$\mathrm{RMSE} = \sqrt{\frac{1}{n}\sum_{i=1}^{n}(y_i - \hat{y}_i)^2} \tag{8}$$

- Coefficient of Determination (R^2): indicates the proportion of variance in the strain measurements explained by the model.

$$R^2 = 1 - \frac{\mathrm{SSR}}{\mathrm{SST}} \tag{9}$$

where SSR and SST are the sum of squares regression and the sum of squares total, respectively, and are given by:

$$SSR = \sum_{i=1}^{n} (\hat{y}_i - \overline{y})^2 \quad (10)$$

$$SST = \sum_{i=1}^{n} (y_i - \overline{y})^2 \quad (11)$$

where y_i is the actual value (true value) of the dependent variable for the i-th observation, $\hat{y}_i$ is the predicted value of the dependent variable for the i-th observation, generated by the model, n is the total number of observations (data points) in the dataset and $\overline{y}$ is the mean of the actual values

Figure 18 compares the predicted strain values with the actual strains from the test set for the strain gauge position number 2.

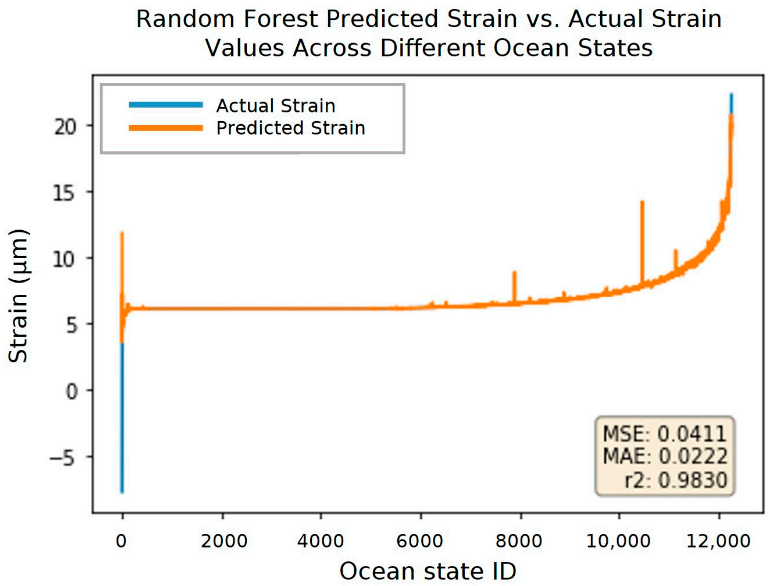

Figure 18. Comparison of the random forest regressor's predicted and actual strain values across various ocean states for strain gauge position number 2.

The model achieved an average R^2 score of 0.96 across all 15 strain outputs, demonstrating high predictive accuracy. The MSE and RMSE values were acceptably low, indicating that the model effectively captured the nonlinear relationships between the oceanographic parameters and the structural strains. The performance metrics of the decision tree regressor algorithm, with averaged results across all strain variables, are provided in Table 14.

Table 14. Performance metrics for decision tree regressor algorithm. Averaged results considering all strain variables.

Metric	Value
Global MSE	0.012
Global R^2	0.96
Computational Time	5.4 min

5.3.2. Artificial Neural Network: Multilayer Perceptron

Various architectures are typically developed for specific data types and tasks in artificial neural networks. Convolutional Neural Networks (CNNs) handle spatial data, making them ideal for image and video analyses. Recurrent Neural Networks (RNNs) excel in processing sequential data, such as time series or natural language. However, when it comes to generic regression problems, Multilayer Perceptrons (MLPs) often emerge as a superior choice. MLPs, with their layered structure and fully connected nodes, are good at modelling complex nonlinear relationships without the specialised data preprocessing required by CNNs or RNNs. This simplicity, coupled with their capability to approximate virtually any continuous function, makes MLPs particularly valuable for straightforward regression tasks where interpretability and computational efficiency are key [6]. An ANN is accurate if its predictions are equal to or extremely close to the actual outputs associated with a specific event. Predictions are evaluated using loss functions, and the algorithm optimises network weights and biases to minimise the loss function.

In this work, Mean Squared Error (MSE) was the most suited loss function for the problem. Mean Squared Error (MSE) is particularly effective as a loss function for regression because it emphasises larger errors more than smaller ones, which helps in reducing variance and improving the model's generalisation on unseen data. Additionally, minimising MSE during training directly correlates with maximising the R^2 score, as R^2 essentially measures the proportion of variance in the dependent variable that is predictable from the independent variables, and a lower MSE indicates a higher proportion of explained variance, thereby increasing the R^2 value.

To optimise the network's weights in such a way that the loss function is minimised, backpropagation is employed, a method that ensures the network learns effectively from its errors. As previously explained, a forward pass process happens when training MLPs where input data are passed through the network, layer by layer, until they reach the output layer where the final predictions are made. Then, the error is quantified through the loss function, providing a starting point for adjustments to improve network accuracy.

MLPs are flexible neural networks with several parameters that can be adjusted. It is essential to identify the optimal parameters for a specific dataset using the validation dataset. Optuna was employed to optimise the hyperparameters of the neural network model. The optimisation process considered variables such as the number of layers, units per layer, activation functions, dropout rates, optimiser types, learning rates, epochs and batch sizes. By dynamically adjusting these hyperparameters, Optuna determined the optimal values that effectively minimised the validation loss on the validation dataset. This automated approach facilitated efficient exploration of the hyperparameter space, enhancing model performance without the need for manual tuning [28].

As detailed in Table 15, the best-performing MLP model included deeper layers, a change in activation function and a different optimizer, resulting in significantly improved performance metrics, including a lower RMSE and a better R^2 score.

Table 15. Hyperparameters and results from the GridSearch optimisation and the best-performing MLP model.

	Best MLP
Nº Hidden Layers	2
First Hidden Layer	831
Second Hidden Layer	978
Epochs	227,204
Activation Function	Leaky ReLU
Optimisation Algorithm	Adam
Learning Rate	0.008480
Batch size	645
Global RMSE	0.00601
Global R^2	0.99957

Figure 19 compares the predicted strain values with the actual strains from the test set.

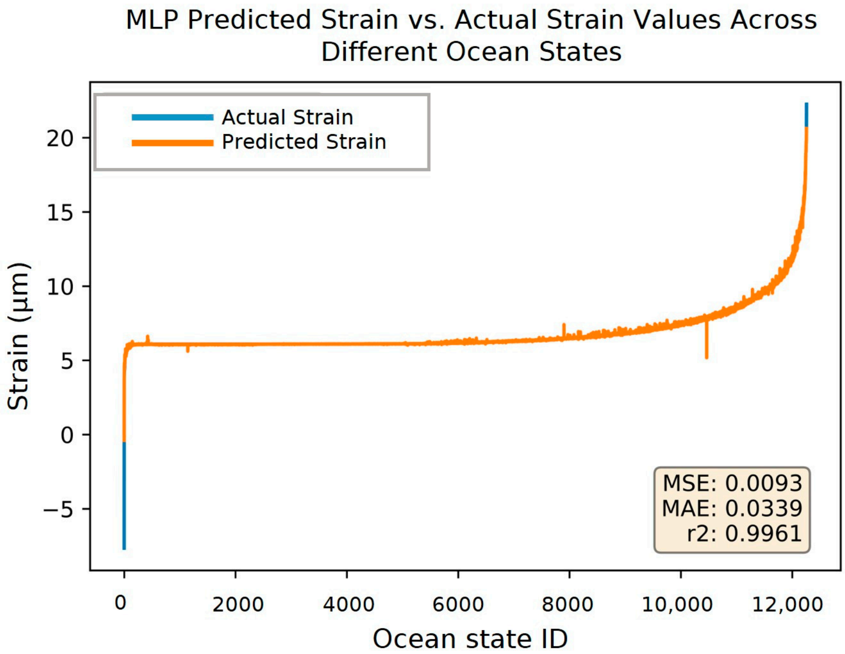

Figure 19. Comparison of predicted and actual strain values from the MLP model across various ocean states for strain gauge position number 2.

6. Discussion

This study aimed to develop a machine learning model for predicting structural damage in submerged structures due to ocean waves and currents. By combining numerical simulations and machine learning (ML) techniques, the effectiveness of these approaches for Structural Health Monitoring (SHM) applications was assessed. The goal was to generate reliable models that could predict critical structural responses, such as stress and strain, under marine conditions and the process of generating reliable data for training purposes.

When comparing strain predictions between current-only scenarios and specific sea states, the correlation between the analytical and FEM method and the FSI simulations demonstrates general consistency in the high- and low-strain regions. This agreement is crucial, as it indicates that the analytical and FEM method, despite their simplifications, capture key trends in the structural response. However, the discrepancies observed on the horizontal plates highlight limitations in the analytical approach, mainly due to assumptions made about load distribution.

The two proposed machine learning approaches presented very good results and are detailed in Table 16. This table provides a direct comparison of the models, illustrating their performance in terms of accuracy, computational efficiency and complexity.

The performance metrics of the evaluated machine learning models highlight trade-offs between accuracy, computational efficiency and the ability to handle different data patterns. Random forest regressors can capture complex patterns, offering high accuracy with a low computation time. Finally, the MLP delivered the highest accuracy but required significant computational resources (2 days) and an even higher development time. These results underscore the importance of selecting models that align with the complexity and patterns of the available data, ensuring that the chosen algorithms can capture the underlying relationships while maintaining computational feasibility in AI development for SHM.

Table 16. Performance comparison of machine learning algorithms studied.

Algorithm	R^2	RMSE	Training Computational Time	Hyperparameters
Random Forest	0.960	0.012	5.4 min	Number of estimators, maximum depth, minimum samples split, maximum features
MLP	0.995	0.011	2 days	Loss functions, optimization algorithms, learning rate, number of layers and neurons, among others

The reliability of machine learning models is fundamentally dependent on the quality and diversity of the data used during training. While empirical methods, such as real-scale experiments, provide the most realistic and accurate data, their high cost and logistical challenges often limit their use in extensive studies. In this study, numerical methods, including CFD and FEM simulations, were used to generate large volumes of training data efficiently. These methods offer a viable alternative, allowing the modelling of complex systems that reduce reliance on physical experiments. However, the importance of empirical validation cannot be overstated.

Future work will focus on the analysis of the experimental data collected from the benthic lander, which will be essential for validating the machine learning models originally trained with numerical data. This validation is essential to confirm the models' ability to predict structural responses under real-world marine conditions. Subsequently, a new machine learning model will be developed and trained using the experimental data in order to enhance the model's predictive accuracy. In parallel, further work is necessary to optimise the computational domain for future Fluid–Structure Interaction (FSI) simulations, balancing accuracy with computational efficiency.

While the framework proposed in this study was designed for a specific structure within the Marewind project, improving the generalizability of SHM models remains an important challenge. Future research is needed to develop methodologies to expand the applicability of these models to diverse structures and operational conditions, ensuring their robustness and adaptability.

Author Contributions: A.B.d.S. and H.M.V.: Conceptualization, methodology, validation, investigation, writing—original draft preparation. R.F.F.L., M.L.P.P., M.T. and A.M.S.C.: Conceptualization. S.D., P.J.S.C.P.S. and T.M.R.M.D.: Conceptualization, writing—review and editing, supervision. P.M.G.P.M.: Project administration. All authors have read and agreed to the published version of the manuscript.

Funding: This work was developed in the scope of the project "MAREWIND—Materials solutions for cost Reduction and Extended service life on WIND offshore facilities", which has received funding from the European Union's Horizon 2020 research and innovation programme under grant agreement N° 952960. The author Rogério F. F. Lopes gratefully acknowledges the "Fundação para a Ciência e a Tecnologia" (FCT) for the funding of the PhD scholarship 2022.13216.BD.

Data Availability Statement: Restrictions apply to the availability of these data. Data were obtained from Hydrographic Institute of Portugal and are available upon request directly to the Hydrographic Institute of Portugal.

Acknowledgments: The authors would like to thank the Hydrographic Institute of Portugal for their invaluable support in the experimental work, including the deployment and retrieval of the benthic lander, as well as their contribution of resources, which greatly enhanced the success of the experimental work.

Conflicts of Interest: The authors declare no conflicts of interest.

References

1. Pengfei, L.; Dong, X. 1—AE health monitoring technique for composite wind turbine blade: A state-of-art review. In *Acoustic Emission Signal Analysis and Damage Mode Identification of Composite Wind Turbine Blades*; Liu, P., Ed.; Elsevier: Amsterdam, The Netherlands, 2023; pp. 1–37. Available online: https://www.sciencedirect.com/science/article/pii/B9780323886529000042 (accessed on 29 May 2024).
2. Silva-Campillo, A.; Pérez-Arribas, F.; Suárez-Bermejo, J.C. Health-Monitoring Systems for Marine Structures: A Review. *Sensors* **2023**, *23*, 2099. [CrossRef] [PubMed]
3. Jiang, K.; Han, Q.; Du, X.; Ni, P. Structural dynamic response reconstruction and virtual sensing using a sequence to sequence modeling with attention mechanism. *Autom. Constr.* **2021**, *131*, 103895. [CrossRef]
4. Dasari, K.; Dogra, A. Designing a Virtual Twin for Structural Health Monitoring by Integrating BIM and Digital Twin Framework. In *Low Carbon Materials and Technologies for a Sustainable and Resilient Infrastructure*; Pancharathi, R.K., K.Y. Leung, C., Chandra Kishen, J.M., Eds.; Springer Nature: Singapore, 2024; pp. 263–278.
5. Van Rijn, L.C. Unified View of Sediment Transport by Currents and Waves. I: Initiation of Motion, Bed Roughness, and Bed-Load Transport. *J. Hydraul. Eng.* **2007**, *133*, 649–667. [CrossRef]
6. Zhang, N.; Chang, Y.; Shi, J.; Chen, G.; Zhang, S.; Cai, B. Fragility assessment approach of deepwater drilling risers subject to harsh environments using Bayesian regularization artificial neural network. *Ocean Eng.* **2021**, *225*, 108793. [CrossRef]
7. Giurgiutiu, V. 1—Introduction. In *Structural Health Monitoring*; Giurgiutiu, V., Ed.; Academic Press: Burlington, NJ, USA, 2008; pp. 1–11. Available online: https://www.sciencedirect.com/science/article/pii/B9780120887606500027 (accessed on 29 May 2024).
8. Karadeniz, H.; Saka, M.P.; Togan, V. Water Wave Theories and Wave Loads. In *Stochastic Analysis of Offshore Steel Structures: An Analytical Appraisal*; Karadeniz, H., Ed.; Springer: London, UK, 2013; pp. 177–252. [CrossRef]
9. Mehaute, B.L. *An Introduction to Hydrodynamics and Water Waves*; Springer Science & Business Media: Berlin/Heidelberg, Germany, 2013.
10. OpenStreetMap Contributors. OpenStreetMap 2024. Available online: https://www.openstreetmap.org (accessed on 2 December 2024).
11. Chakrabarti, S.K. *Hydrodynamics of Offshore Structures*, 3rd ed.; revised reprint; Computational Mechanics: Plainfield, IL, USA, 1987.
12. Clauss, G.; Lehmann, E.; Östergaard, C. *Offshore Structures*; Springer: London, UK, 1992. Available online: http://link.springer.com/10.1007/978-1-4471-3193-9 (accessed on 11 June 2024).
13. Galdi, G.P. An Introduction to the Navier-Stokes Initial-Boundary Value Problem. In *Fundamental Directions in Mathematical Fluid Mechanics*; Galdi, G.P., Heywood, J.G., Rannacher, R., Eds.; Birkhäuser: Basel, Switzerland, 2000; pp. 1–70. [CrossRef]
14. Kim, S.-Y.; Kim, K.-M.; Park, J.-C.; Jeon, G.-M.; Chun, H.-H. Numerical simulation of wave and current interaction with a fixed offshore substructure. *Int. J. Nav. Archit. Ocean Eng.* **2016**, *8*, 188–197. [CrossRef]
15. Marques Machado, F.M.; Gameiro Lopes, A.M.; Ferreira, A.D. Numerical simulation of regular waves: Optimization of a numerical wave tank. *Ocean Eng.* **2018**, *170*, 89–99. [CrossRef]
16. Ning, D.Z.; Teng, B. Numerical simulation of fully nonlinear irregular wave tank in three dimension. *Int. J. Numer. Methods Fluids* **2007**, *53*, 1847–1862. [CrossRef]
17. Silva, M.C.; Vitola, M.; Pinto, W.T.; Levi, C. Numerical simulation of monochromatic wave generated in laboratory: Validation of a cfd code. In Proceedings of the 23 Congresso Nacional de Transport Aquaviario Construcao naval Offshore, Rio de Janeiro, Brazil, 25–29 October 2010; pp. 1–12.
18. Havn, J. Wave Loads on Underwater Protection Covers. 2011. Available online: https://ntnuopen.ntnu.no/ntnu-xmlui/handle/11250/238072 (accessed on 17 April 2024).
19. Zore, K.; Sasanapuri, B.; Parkhi, G.; Varghese, A. Ansys mosaic poly-hexcore mesh for high-lift aircraft configuration. In Proceedings of the 21st AeSI Annual CFD Symposium, Bangalore, India, 8–9 August 2019.
20. Ansys Mosaic Technology Combines Disparate Meshes. Available online: https://www.ansys.com/resource-center/white-paper/ansys-fluent-mosaic-technology (accessed on 18 April 2024).
21. Arocena, V.M.; Danao, L.A.M. Improving the Modeling of Pressure Pulsation and Cavitation Prediction in a Double-Volute Double-Suction Pump Using Mosaic Meshing Technology. *Processes* **2023**, *11*, 660. [CrossRef]

22. Aldoseri, A.; Al-Khalifa, K.N.; Hamouda, A.M. Re-Thinking Data Strategy and Integration for Artificial Intelligence: Concepts, Opportunities, and Challenges. *Appl. Sci.* **2023**, *13*, 7082. [CrossRef]
23. Goodfellow, I. *Deep Learning*; MIT Press: Cambridge, MA, USA, 2016.
24. Breiman, L. Random forests. *Mach. Learn.* **2001**, *45*, 5–32. [CrossRef]
25. Cabello-Solorzano, K.; Ortigosa de Araujo, I.; Peña, M.; Correia, L.; Tallón-Ballesteros, A.J. The Impact of Data Normalization on the Accuracy of Machine Learning Algorithms: A Comparative Analysis. In Proceedings of the 18th International Conference on Soft Computing Models in Industrial and Environmental Applications (SOCO 2023), Salamanca, Spain, 5–7 September 2023; García Bringas, P., Pérez García, H., Martínez de Pisón, F.J., Martínez Álvarez, F., Troncoso Lora, A., Herrero, Á., Calvo Rolle, J.L., Quintián, H., Corchado, E., Eds.; Springer Nature: Cham, Switzerland, 2023; pp. 344–353.
26. sklearn.preprocessing.StandardScaler. Scikit-Learn. Available online: https://scikit-learn.org/stable/modules/generated/sklearn.preprocessing.StandardScaler.html (accessed on 19 April 2024).
27. 3.4. Metrics and scoring: Quantifying the Quality of Predictions. Scikit-Learn. Available online: https://scikit-learn.org/stable/modules/model_evaluation.html (accessed on 28 November 2024).
28. Optuna—A Hyperparameter Optimization Framework. Optuna. Available online: https://optuna.org/ (accessed on 21 October 2024).